

Buoyant flexure and basal crevassing in dynamic mass loss at Helheim Glacier

Timothy D. James^{*}, Tavi Murray, Nick Selmes, Kilian Scharrer and Martin O'Leary



Iceberg calving accounts for a significant proportion of annual mass loss from marine-terminating glaciers^{1,2} and may have been a factor in the rapid demise of ancient ice sheets³. The largest contributions from the main outlet glaciers of the Greenland ice sheet to sea-level rise over the next two centuries have been projected to be dynamic in origin, that is, driven by glacier flow and calving⁴. However, present physical models remain a coarse approximation of real calving mechanisms because models are poorly constrained by sparse glacier geometry observations⁵. Here we present a record of daily digital elevation models from the calving margin of Greenland's Helheim Glacier at a high spatial resolution. Our digital elevation models are derived from stereo terrestrial photography taken over the summers of 2010 and 2011. We find that during these two summers dynamic mass loss at Helheim Glacier was dominated by calving events exceeding 1 km³ that were the result of buoyant flexure and the propagation of basal crevasses. We suggest that this buoyancy-driven mechanism for calving may be common elsewhere in Greenland and could be a first-order control on the ice sheet's future contribution to sea-level rise.

Glacier models originally parameterized iceberg calving using an independent variable such as water depth (for example, ref. 6). Subsequently, empirical relationships were linked to physical properties of the glacier using the height-above-buoyancy criterion. Here calving front position occurs where ice thickness reaches some height threshold above flotation and calving rate becomes a function of ice flux to the terminus^{3,7}. However, neither approach can reproduce the range of behaviour typical of a large marine-terminating glacier such as Helheim⁵. Models that define calving front location as the point where transverse surface crevasses propagate to the waterline have been more successful at simulating the wide variety of calving behaviour⁸. Although a simplification, crevasse depth is widely considered to be a first-order control on calving rate with terminus position ultimately a function of ice velocity, strain rate, ice thickness and water depth. The crevasse-depth model has been extended to include the sensitivity of calving rate to a depth of water in surface crevasses^{8–10} and also the propagation of basal crevasses⁵. These advances have enabled the modelling of individual calving events¹⁰ as well as the development of models that use assumed realistic and fully dynamic marine boundary conditions for forecasting of sea-level contributions⁴. However, owing in large part to a lack of observational data, the true mechanisms of calving are still largely unknown and thus the development of a universal calving law remains unresolved.

Our high-temporal- and spatial-resolution time series of digital elevation models (DEMs) of the Helheim calving margin (Supplementary Fig. 1) using stereo, terrestrial time-lapse photography (see Methods, Terrestrial and ASTER photogrammetry) gives a detailed account of the evolution of

the glacier terminus here presented in 24-h time steps. In 2010, Helheim experienced four major calving events between 11 and 30 July with a cumulative areal loss of ~5.06 km² (~8.0 km² extrapolated beyond camera viewshed; Fig. 1).

The daily evolution of the calving front is shown in longitudinal profiles along the main flowline of the glacier (Fig. 2). The most striking feature (Fig. 2a) is the large surface depression some 20–30 m in depth running parallel to, and about 1.5 km up-glacier from the 11 July calving front. This depression developed over the weeks preceding calving during a period of no major calving activity. Depressions such as this have been reported previously in the literature and have been attributed to dynamic thinning associated with glacier retreat down a reverse bed slope^{11,12}.

On the first day of the time series, the front advanced (~22 m), lifted (~5 m) and the depression advected downstream at approximately the speed of ice flow (Fig. 2a). The glacier then experienced three significant calving events in close succession resulting in the glacier front retreating to the surface depression. The first of these calving events was captured in high resolution 10 s time-lapse imagery, which shows the formation of a backward-rotating iceberg measuring >4 km across-glacier and 300 m in the direction of glacier flow (Supplementary Movie 2). Over the next 14 days (Fig. 2b) the terminus advanced daily without calving during which time the front lifted, slowly at first, accelerating vertically (from 0 to ~8 m d⁻¹) as the next calving event approached. Over this period, the surface again became depressed to a depth of ~20 m below the height of the calving front about 400 m up-glacier from the terminus. Note the images show that the depression was not the result of an expanding rift(s) but rather the downward flexure of the surface coupled with the lifting front; evidence that the section down-glacier of the depression was under rotation while still attached to the main glacier. On the last day of the time series, the fourth calving event occurred. The front again retreated to the depression and the surface rebounded vertically to its previous height suggesting that the ice, while under rotation, was being held below flotation.

We applied feature tracking (see Methods, Feature tracking) to the daily images before the 12 July 2010 calving event to demonstrate the visible vertical displacement of the glacier that occurs across the entire visible calving front (Fig. 3). The lifting of the front and formation of the associated depression are clearly discernible in the imagery days before the iceberg detaches. Figure 3 and the profiles in Fig. 2b show that the rotation of the front section accelerates as a calving event nears and ultimately leads to ice failure and calving. Poor lighting before the 29 July 2010 calving event prohibited image use in feature tracking; however, the same rotational mechanism of calving was visible.

A short time series of elevation profiles from 2011 (Fig. 2c) shows that the glacier advanced beyond the location of the 2010 depression with no frontal uplift despite the similar thickness of the

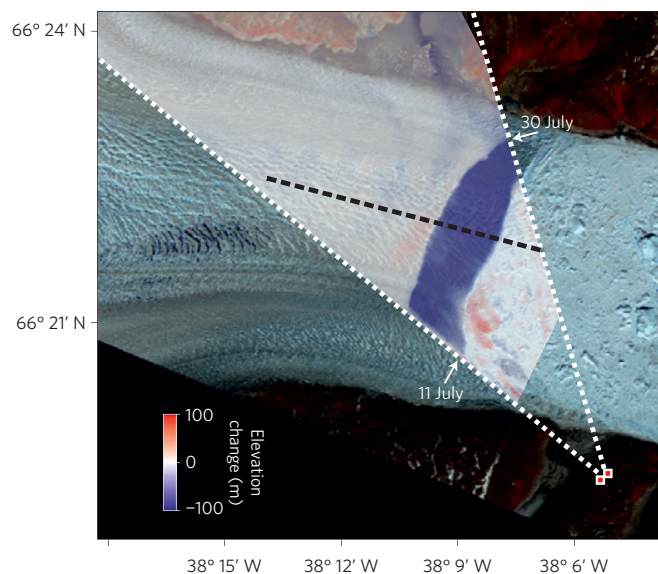


Figure 1 | Camera locations with differenced DEMs. Camera stations plotted on 8 July 2010 ASTER image. Figure 2 profile (black dashed line) and approximate camera viewshed are shown. Elevation changes at Helheim from 11 to 30 July 2010 (front positions indicated) are overlaid showing ice loss of $\sim 4.0 \text{ km}^2$ in the cameras' viewshed and $\sim 0.29 \text{ km}^3$ above sea-level volume loss. Negative change anomalies in the top right are errors associated with mountain shadow. Large elevation changes in the ice mélange show movement of icebergs in the fjord and production of new icebergs by the calving events.

glacier. However, feature tracking applied to the images leading up to four major 2011 calving events reveals that the same rotational movement with lifted front and downward flexure of the surface preceded calving throughout the 2011 summer (Supplementary Figs 3–5). The frontal evolution we describe can be seen in a series of photographs from the southern side of the glacier where the surface is in plain view, closer to the cameras and well lit over the 6-day sequence (Supplementary Fig. 6). Although we do not have data to support this, we anticipate compression in the hinge zone amidst the overall extensional flow of the Helheim terminus.

Understanding this behaviour requires a longer-term context as well as bed topography. ASTER surface profiles show that surface depressions with a high calving front occur often and at a number of positions in the fjord (Fig. 4, see Methods, Terrestrial and ASTER photogrammetry) although a single image cannot reveal whether the front was undergoing rotation. An exception is the 18 July 2004 ASTER scene that captured a clearly rotated front section with the normally vertical calving face visible in the satellite image owing to its high rotation angle as the next calving event approached (Supplementary Fig. 7). We also analysed the available bed data at the Helheim terminus (see Supplementary Methods, Bed Topography) and show mean vertical errors at crossover points between lines of 40 m with errors up to 200 m near the calving front (Supplementary Fig. 8). Bed points within 100 m of our surface profiles are shown with ASTER elevation profiles in Fig. 4. Although there is some agreement that the bed slopes down-glacier above km 4.2, as labelled on the x axis of Fig. 4, the bed topography at the 2010/2011 calving front location is uncertain. Whereas the 2001 and 2008 lines suggest a reverse bed slope, the 2011 and 2013 profiles suggest a gentle down-glacier slope.

The glacier climbing up a reverse bed slope could account for the apparent rotation of these calving sections. However, there is some evidence that the ice in these areas is not grounded. Global Positioning System data that are spatially and temporally

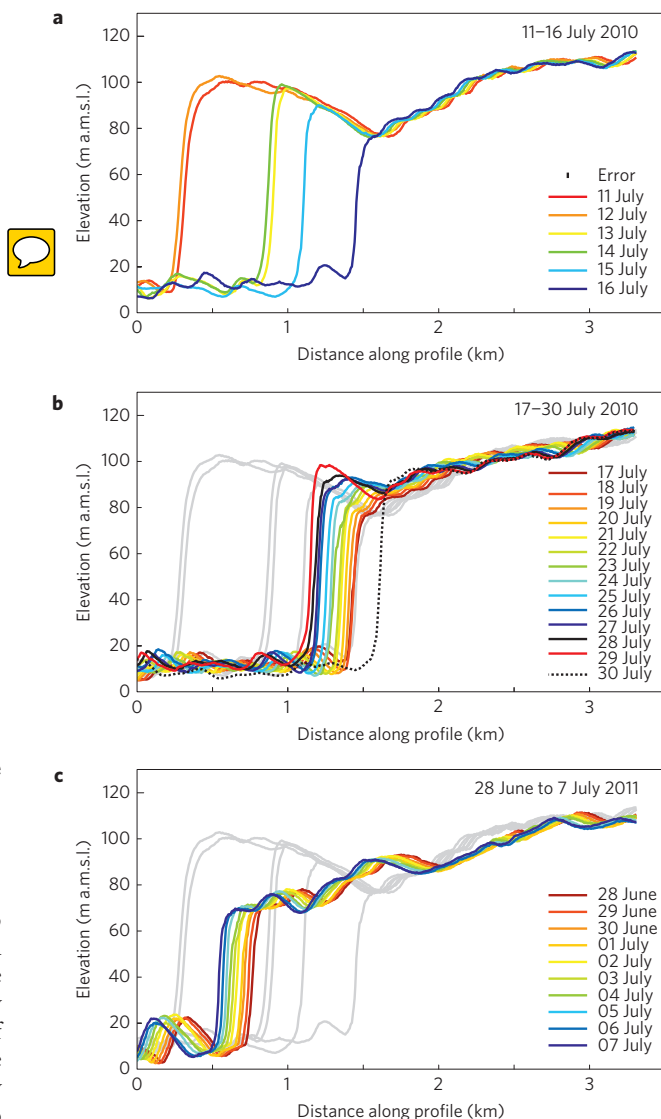


Figure 2 | Elevation profiles along Helheim's central flowline. **a**, During the first six days the glacier terminus underwent three significant calving events causing the front to retreat to a pre-existing depression, which the ASTER record shows deepened over the preceding period of minimal frontal activity. **b**, Over the next 14 days, as the terminus advanced, the front lifted and a depression formed to which the front retreated on the last day of this time series. **c**, In 2011, the front lies over the location of the 2010 depression without any sign of a similar surface high or low. Grey lines in **b, c** show elevation profile from **a**.

coincident with a 2007 laser altimeter profiles (Fig. 4) show that the front of Helheim is tidally influenced during the build-up to these calving events¹³. In addition, this style of calving also occurs on the south side of the fjord (Supplementary Fig. 8) where the bed data indicate a down-glacier bed slope. Therefore, we seek an alternative explanation.

There is considerable literature on buoyancy-induced rotation at marine and lacustrine termini (ref. 14). Buoyancy forces increase when a grounded glacier's terminus is lowered relative to water height, becoming increasingly out of buoyant equilibrium. This requires ice rotation to restore equilibrium, which can occur either slowly by creep or rapidly by fracture propagation. Studies have shown that increasing buoyancy can occur when high rates of surface ablation cause ice to thin below flotation¹⁵. However, recent models estimate average summer ablation rates of only

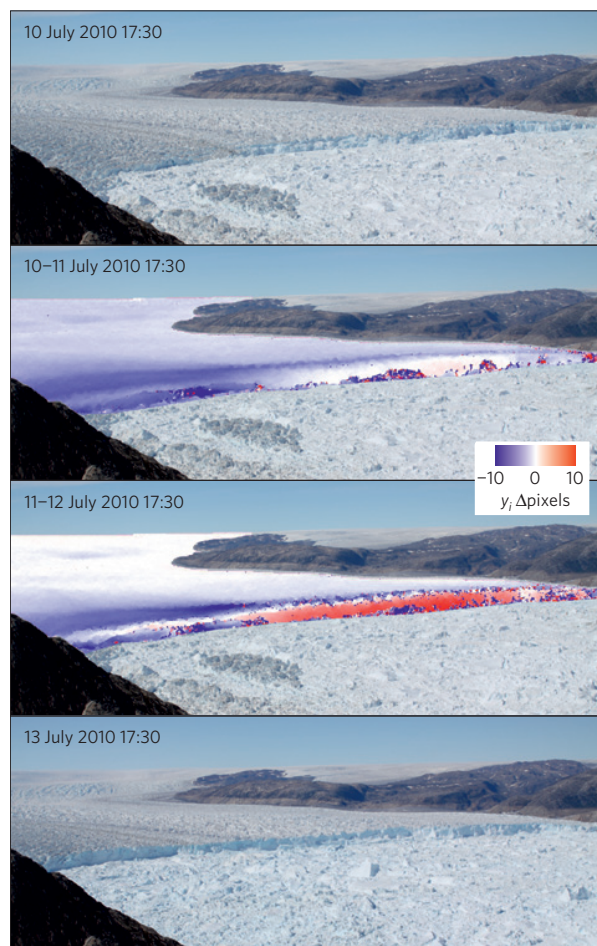


Figure 3 | Image feature tracking before 12 July 2010 18:30 UTC calving event. This event was a full-width/full-depth calving event and was captured in 10 s time lapse (Supplementary Movie 2). We applied feature tracking methods to the imagery over two 24-h periods before calving to show the displacement at the calving front. Units are in pixels of displacement in image space (along y_1 axis; see Methods) with positive up, approximating vertical movement in real space. Error is ~ 1 pixel.

$\sim 0.055 \text{ m d}^{-1}$ at Helheim's terminus¹⁶. Also, the weak seasonal signal to calving at Helheim (in contrast to Kangerdlugssuaq Glacier^{17,18}) suggests that a seasonal driver such as surface melting is not responsible.

Surface depressions are characteristic of ice-shelf grounding lines; where a glacier transitions from grounded to floating ice^{19,20}. The evolution of the front in Supplementary Fig. 6 and Fig. 2b, in particular the vertical rebounding of the glacier after a calving event, suggests that the ice is being held below flotation either owing to the rotation itself or as a consequence of another process. We propose that given the high speed of the glacier at the calving margin ($> 20 \text{ m d}^{-1}$), this could represent the glacier being driven below flotation as it flows into deeper water at a rate faster than it can adjust. However, this mechanism could hold on a reverse bed slope only if rates of subglacial melting or dynamic thinning were high. Alternatively, at the grounding line, basal drag is rapidly lost creating high longitudinal stress gradients and down-glacier stretching. The consequent dynamic thinning could cause the glacier to thin below flotation in a similar way and although ungrounding of the glacier would be encouraged by a down-glacier bed slope it is not prerequisite to the process.

In any case, basal crevasses, expected in areas with high longitudinal strain rates and low basal effective pressure²¹, are

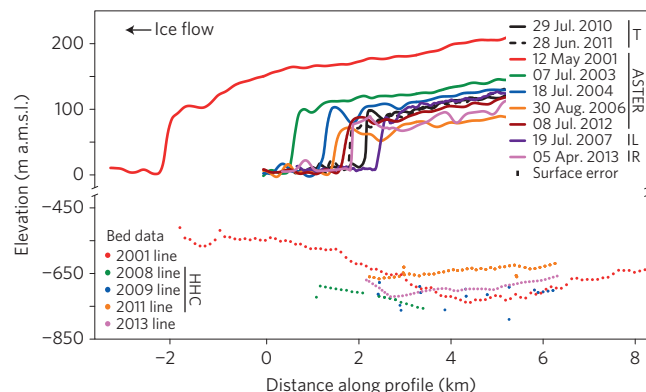


Figure 4 | Surface profiles and bed topography. Surface profiles from terrestrial imagery (T), ASTER, lidar (L) and radar (R) with 2001 and 2013 bed lines and the CReSIS 2008–2012 Helheim Composite (HHC) bed product. Whereas the 2001 and 2008 lines suggest a reverse bed slope, the more recent lines, collected with the Multichannel Coherent Radar Depth Sounder, show a down-glacier slope. The upward inflection in 2013 coincides with the rotated 2013 calving front, suggesting that the ice base is not in contact with the fjord bed at this location. The 2009 crossover lines show the significant error in the bed data.

important in determining the location of calving. Additional factors, such as ice velocity, bed slope, and surface, basal and frontal melting, will vary over space and time, contributing to the iceberg aspect ratio, key in determining the style of calving²². This is illustrated by the 12 August 2011 event (Supplementary Fig. 5) where an overturning iceberg calved on the south side of the fjord after several days of strong rotation whereas on the north side a tabular iceberg calved with no visible uplift but some evidence of downward flexure in the images. Submarine melt in particular, linked to fjord temperatures and circulation, has been shown to have an important amplifying effect on calving²³.

Understanding the mechanisms behind large calving events is vital for producing reliable models that forecast Greenland's future contribution to sea level. Models that reproduce observed glacier behaviour over relatively short timescales using bed data with large errors may result in high uncertainty when extrapolated into the future especially if also not based on the correct physical processes. We provide improved observations of calving during two summers at Helheim Glacier giving a detailed characterization of large calving events. Our results show that large, overturning icebergs begin rotating under buoyancy forces several days before detachment from the glacier. It is clear that the propagation of air and water-filled surface crevasses, which has previously been used as a first-order approximation of calving^{8,10}, does not drive calving over this period. Rather, the propagation of basal crevasses driven by buoyant flexure seems to have dominated dynamic mass loss at Helheim. Improving our understanding of longitudinal and buoyancy forces, their role in basal crevasse initiation, propagation and iceberg production, and their use in time-evolving calving models is key to reducing uncertainty of future sea-level contributions from the Greenland ice sheet.

Methods

Terrestrial and ASTER photogrammetry. In the summers of 2010 and 2011, we installed two 15.1 megapixel Canon 50D digital single-lens reflex cameras on the south shore of Helheim Fjord $\sim 300 \text{ m}$ apart and $\sim 3.5 \text{ km}$ down-fjord from the 2010 calving front (Fig. 1). We used fixed 28 mm focal length lenses, which are sufficiently wide-angle to capture most of the glacier terminus from this distance with minimal distortion. Camera viewsheds and image overlap, which enables the extraction of elevation models, are shown in Fig. 1. The cameras were manually synchronized and set to take an image every 60 min. Clock drift was $< 15 \text{ s}$ over a period of several months. In 2010, the cameras ran from 11 to 30 July (20 days,

~500 image pairs). In 2011, 11 days of stereo imagery were collected from 27 June to 8 July owing to a power failure in one camera but mono imagery was collected to 29 August (64 days, ~1,500 images).

Daily DEMs were generated using images taken at 8:30 UTC owing to optimal lighting of the calving front. Camera calibration was used to model and minimize focal length and lens distortion errors. Ground control points (GCPs), which link two-dimensional (2D) image space to 3D ground space were extracted from stable areas of a 2007 lidar DEMs following the methodology in refs 24,25. DEMs were produced from stereo imagery using the 3D viewing capabilities of the SocetSET digital photogrammetry suite, which is key for measuring the GCP in the images. The photogrammetric bundle adjustment and DEM extraction was undertaken in Topcon's ImageMaster.

DEMs were extracted nominally on a 5 m grid, where image resolution permitted because image resolution decreases with distance from the cameras in oblique imagery. These factors as well as the complicated surface topography meant the resulting topographic model took the form of an irregular cloud of X , Y , Z coordinate triplets with a maximum resolution of 5 m that decreases with increasing distance from the cameras. To simplify processing, point clouds were interpolated to a 10 m grid using a local polynomial approach that assigns grid values using a weighted least-squares fit to data within a user-specified search window of 200 m. This window size preserved sufficient surface detail for comparison while eliminating higher frequency elevation variations. An example DEM is given in Supplementary Fig. 1 and data quality is addressed in Supplementary Methods.

We produced DEMs from stereo ASTER imagery at 50 m resolution using SocetSET's ASTER sensor model. Although it is theoretically possible to produce ASTER DEMs at the same resolution as the imagery (15 m), quality control of such a large and dense data set on such an irregular surface is difficult and unnecessary for characterizing the important changes at Helheim. As with the terrestrial photographs, GCPs were extracted from the 2007 lidar DEM. The average root mean square error of the photogrammetric block adjustment was 5.2 m in X , Y and 1.1 m in Z suggesting a good fit of the sensor model to the image measurements. Owing to the low resolution of ASTER imagery the quality of the resulting DEM will be lower than the root mean square error of the model fit to image measurements. Quality will also be negatively affected by poor image contrast on dark and bright surfaces. We estimate planimetric error to be ± 8 m and elevation error in the ASTER DEMs to be ± 2.5 m.

Feature tracking. A large amount of spatial information can be recorded in photographs, which becomes evident when manually 'flicking' through a time series. To provide a simple means of quantifying the evolution of the Helheim calving front, we used the California Institute of Technology's COSI-Corr orthorectification and feature tracking module²⁶. COSI-Corr was developed primarily for satellite and airborne images (that is, near-vertical or nadir viewing angle) and typically, images are orthorectified before image correlation to provide displacements in ground coordinates. The orthorectification of high-oblique imagery is difficult and was unnecessary for demonstrating the vertical displacement at the calving front. COSI-Corr outputs the x and y components of displacement in image space (x_i , y_i). In this image configuration, ice displacement at the calving front due to glacier flow is dominantly along the x_i image axis. Therefore, we approximate vertical ice displacement using movement along the y_i axis. This assumption degrades towards the left side of the image where there is a larger component of glacier flow along the y_i axis, but the rotation of the front section remains clearly visible. Displacement measured on the stationary mountains suggests that the error in these figures is ~1 pixel.

Received 26 September 2013; accepted 13 June 2014;
published online 13 July 2014

References

- Hagen, J. O., Kohler, J., Melvold, K. & Winther, J. G. Glaciers in Svalbard: Mass balance, runoff and freshwater flux. *Polar Res.* **22**, 145–159 (2003).
- Rignot, E. & Kanagaratnam, P. Changes in the velocity structure of the Greenland ice sheet. *Science* **311**, 986–990 (2006).
- Van der Veen, C. J. Calving glaciers. *Prog. Phys. Geogr.* **26**, 96–122 (2002).
- Nick, F. M. *et al.* Future sea-level rise from Greenland's main outlet glaciers in a warming climate. *Nature* **497**, 235–238 (2013).
- Nick, F. M., Van der Veen, C. J., Vieli, A. & Benn, D. I. A physically based calving model applied to marine outlet glaciers and implications for the glacier dynamics. *J. Glaciol.* **56**, 781–794 (2010).
- Meier, M. F. & Post, A. Fast tidewater glaciers. *J. Geophys. Res.* **92**, 9051–9058 (1987).
- Van der Veen, C. J. Tidewater calving. *J. Glaciol.* **42**, 375–385 (1996).
- Benn, D. I., Hulton, N. R. J. & Mottram, R. H. 'Calving laws', 'sliding laws' and the stability of tidewater glaciers. *Ann. Glaciol.* **46**, 123–130 (2007).
- Vieli, A. & Nick, F. M. Understanding and modelling rapid dynamic changes of tidewater outlet glaciers: Issues and implications. *Surv. Geophys.* **32**, 437–458 (2011).
- Cook, S., Zwinger, T., Rutt, I. C., O'Neil, S. & Murray, T. Testing the effect of water in crevasses on a physically based calving model. *Ann. Glaciol.* **53**, 90–96 (2012).
- Vieli, A., Jania, J. & Kolondra, L. The retreat of a tidewater glacier: Observations and model calculations on Hansbreen, Spitsbergen. *J. Glaciol.* **48**, 592–600 (2002).
- Joughin, I. *et al.* Ice-front variation and tidewater behavior on Helheim and Kangerdlugssuaq Glaciers, Greenland. *J. Geophys. Res.* **113**, F01004 (2008).
- De Juan Verger, J. *Tidewater Glacier Flow of Helheim Glacier, Greenland, 2006–2008, Using High-Rate GPS* PhD thesis, Univ. Barcelona (2011).
- Benn, D. I., Warren, C. R. & Mottram, R. H. Calving processes and the dynamics of calving glaciers. *Earth Sci. Rev.* **82**, 143–179 (2007).
- Boyce, E. S., Motyka, R. J. & Truffer, M. Flotation and retreat of a lake-calving terminus, Mendenhall Glacier, southeast Alaska, USA. *J. Glaciol.* **53**, 211–224 (2007).
- Andersen, M. L. *et al.* Spatial and temporal melt variability at Helheim Glacier, East Greenland, and its effect on ice dynamics. *J. Geophys. Res.* **115**, F04041 (2010).
- Bevan, S. L., Luckman, A. J. & Murray, T. Glacier dynamics over the last quarter of a century at Helheim, Kangerdlugssuaq and 14 other major Greenland outlet glaciers. *Cryosphere* **6**, 923–937 (2012).
- Schild, K. M. & Hamilton, G. S. Seasonal variations of outlet glacier terminus position in Greenland. *J. Glaciol.* **59**, 759–770 (2013).
- Vaughan, D. G. Tidal flexure at ice shelf margins. *J. Geophys. Res.* **100**, 6213–6224 (1995).
- Durand, G., Gagliardini, O., de Fleurian, B., Zwinger, T. & Le Meur, E. Marine ice sheet dynamics: Hysteresis and neutral equilibrium. *J. Geophys. Res.* **114**, F03009 (2009).
- Van der Veen, C. J. Fracture mechanics approach to penetration of bottom crevasses on glaciers. *Cold Reg. Sci. Technol.* **27**, 213–223 (1998).
- Amundson, J. M. *et al.* Ice mélange dynamics and implications for terminus stability, Jakobshavn Isbræ Greenland. *J. Geophys. Res.* **115**, F01005 (2010).
- O'Leary, M. & Christoffersen, P. Calving on tidewater glaciers amplified by submarine frontal melting. *Cryosphere* **7**, 119–128 (2012).
- James, T. D., Murray, T., Barrand, N. E. & Barr, S. L. Extracting photogrammetric ground control from lidar DEMs for change detection. *Photogramm. Rec.* **21**, 310–326 (2006).
- James, T. D. *et al.* Observations of enhanced thinning in the upper reaches of Svalbard glaciers. *Cryosphere* **6**, 1369–1381 (2012).
- Ayoub, F., LePrince, S. & Avouac, J. P. Co-registration and correlation of aerial photographs for ground deformation measurements. *ISPRS J. Photogramm.* **64**, 551–560 (2009).

Acknowledgements

T.D.J. was supported by The Leverhulme Trust Research Leadership Award GLIMPSE Project (F/00391/I) and the Climate Consortium for Wales (C3W). N.S. is supported by NERC (NE/I007148/1). N.S. and K.S. were also supported by The Leverhulme Trust. M.O. was supported by the Welsh Institute for Sustainable Environments (WISE). Field work was funded by The Leverhulme Trust, a Royal Geographical Society-Institute of British Geographers EPSRC Geographical Research Grant (2010/01/10), NERC (NE/I007148/1) and the European Union Seventh Framework Programme [FP7/2007–2013] under grant agreement number 262693 [INTERACT]. ASTER imagery were acquired through NASA's Land Processes Distributed Active Archive Center (LP DAAC) with thanks to Operation IceBridge and B. Krabill. The authors would also like to acknowledge software support from TerraDat Geophysics (ImageMaster) and F. Ayoub (COSI-Corr). We acknowledge the use of bed data from CReSIS generated with support from NSF grant ANT-0424589 and NASA grant NNX10AT68G and their assistance with data analysis.

Author contributions

T.D.J. developed the methodology, undertook the analysis and interpretation and prepared the manuscript. T.M. was the grant-holder and contributed to data collection and interpretation. N.S. and K.S. contributed to methodological development and data collection. M.O. contributed to the interpretation. All authors contributed to the manuscript preparation.

Additional information

Supplementary information is available in the [online version of the paper](#). Reprints and permissions information is available online at www.nature.com/reprints. Correspondence and requests for materials should be addressed to T.D.J.

Competing financial interests

The authors declare no competing financial interests.